Sensors & Actuators: B. Chemical 372 (2022) 132671

Contents lists available at ScienceDirect

Sensors and Actuators: B. Chemical

journal homepage: www.elsevier.com/locate/snb

Significant improvement in the acetone sensing performance of Ag-decorated ZnO porous nanosheets through defect engineering by Li-ion implantation

Minkyung Lee [a,b,1], Hyun-Sook Lee [a,1], Min Young Kim [a], Kyu Hyoung Lee [a,*], Wooyoung Lee [a,*]

[a] Department of Materials Science and Engineering, Yonsei University, 50 Yonsei-ro, Seodaemun-gu, Seoul 03722, the Republic of Korea
[b] Chem-bio Technology Center Team1, Agency for Defense Development, 160 Bugyuseong-daero 488 beon-gil, Yuseong-gu, Daejeon 34060, the Republic of Korea

ARTICLE INFO

Keywords:
Gas sensor
Acetone
Ag-decorated ZnO
Li-ion implantation
Defect engineering

ABSTRACT

Defect engineering by Li-ion implantation has been extensively studied in electrocatalysis, photocatalysis, and energy storage devices. Here, we provide the first experimental evidence that Li-ion implantation improves the acetone sensing performance of ZnO-based sensors. The morphological structure of the solvothermally synthesized Ag-decorated ZnO porous nanosheets (Ag-ZnO PNSs) was controlled by Li-ion insertion/extraction at various discharge voltages. The generation of nanocracks caused by the electrochemical reaction between ZnO and Li significantly improved the sensing performance. The nanocracked Ag-ZnO PNSs had a much higher sensing response (~319) to 10 ppm acetone than the ZnO nanoparticles, bare ZnO PNSs, and bare Ag-ZnO PNSs. At the optimum operating temperature of 400 °C, the low detection limit was 0.1 ppm. The significant improvement in the acetone sensing performance of nanocracked sample is attributed to the simultaneous increase in oxygen vacancies and specific surface area, as well as the Ag catalytic effect. Furthermore, the nanocrack structures were found to be stable even after repeated measurements at high temperatures. Our research found that Li-ion implantation is an effective method for improving the gas sensing performance of metal oxide-based sensors, and that nanocracked Ag-ZnO PNSs can be a promising candidate material for use as acetone sensor applications.

1. Introduction

The demand for gas sensors, which are widely used in chemicals, petroleum, mining, automobiles, and medical devices has increased in recent decades as public awareness of environmental pollution, safety, and health care has grown. Additionally, global demand for miniaturized wireless gas sensors is increasing due to the Internet of Things (IoT), cloud computing, and big data, as well as the integration of gas sensors into home appliances and air quality monitoring. Among the numerous volatile organic compounds (VOCs), acetone is a harmful gas that is easily detected in industrial settings and at home. It can lead to a wide variety of health related issues, including headaches and narcosis. Additionally, acetone has been widely accepted as an important indicator for non-invasive diabetes diagnosis since exhaled concentration of acetone (> 1.8 ppm) in diabetic patients is higher than that in healthy people (< 0.9 ppm) [1]. Therefore, it is critical to develop a highly sensitive acetone-sensing material for safety and health of human populations. The developed high-performance acetone sensors can be used in place of costly and cumbersome analytical instruments such as gas chromatography or selective ion flow tube mass spectroscopy.

Various metal-oxide semiconductor (MOS) materials have been investigated as potential acetone-sensing materials, including ZnO, TiO_2, SnO_2, WO_3, and CuO [2]. Among them, ZnO is one of the most extensively investigated sensing materials due to its high electron mobility, wide bandgap (3.37 eV), high exciton binding energy (60 meV), and high thermal and chemical stability, all of which are required for an ideal acetone gas sensor [3]. Additionally, ZnO has several advantages, including a simple synthesis process and low production cost. Numerous efforts have been made to enhance the sensing performance of ZnO through nanostructures, such as nanorods [4], nanowires [5], nanosheets [6], nanotubes [7], nanoparticles [8], as well as the pore structure [9], resulting in a higher surface-to-volume ratio. Additional

* Corresponding authors.
E-mail addresses: khlee2018@yonsei.ac.kr (K.H. Lee), wooyoung@yonsei.ac.kr (W. Lee).
[1] These authors contributed equally.

https://doi.org/10.1016/j.snb.2022.132671
Received 3 May 2022; Received in revised form 8 September 2022; Accepted 12 September 2022
Available online 13 September 2022

doping methods for transition metals [10,11] and noble metal loading [12,13] have also been developed.

Engineering of structural defects is regarded as one of the most important factors in overcoming or improving the limitations of the physical and chemical properties of semiconducting materials. It has been extensively researched in a variety of semiconductor-based applications, including catalysts [14,15], photoactive devices [16–18], photovoltaic cells [19], and electrode materials for lithium-ion batteries (LIBs) [20,21]. Several defect engineering technologies, such as ion implantation [22] and rapid thermal processing [23] are well established. Particularly, as anode materials for LIBs, MOS with oxygen vacancies such as TiO_2, SnO_2, and MnO_2, effectively improve the cycle stability and rate performance of the batteries [21,24]. ZnO has also been investigated as an anode material for LIBs; however, cyclability was insufficient due to its low electronic conductivity and large volume change during Li insertion/extraction [24]. Oxygen defects generated in ZnO by the Li ion insertion/extraction process, can play an important role in improving the sensing performance in sensing materials.

The sensing properties of Ag-decorated ZnO porous nanosheets (Ag-ZnO PNSs) prepared via the Li-ion implantation method were investigated in this study for the detection of acetone. Ag-ZnO PNSs were used as the intrinsic material to maximize the sensing performance. The morphology and microstructure changes of the as-prepared Ag-ZnO PNSs were investigated in detail using electron microscopy at various discharge voltages. Among the various samples, the Ag-ZnO PNSs with nanocracks (crack width ~2.3 nm) demonstrated an excellent sensing response to 10 ppm acetone. Through surface chemistry analysis, the enhanced response was explained as the result of more surface oxygen vacancies generated in the nanocracks.

2. Materials and methods

2.1. Synthesis of Ag-decorated ZnO porous nanosheets

To begin, 7.2 g of Zn $(NO)_3{\cdot}6\ H_2O$ (Sigma-Aldrich) was dissolved for 30 min in 180 mL of an ethanol-water (1:2) mixture. Then, 3.6 g of urea was added to the mixture and stirred for 30 min to ensure uniform mixing. Finally, 3.0 wt% of $AgNO_3$ (Sigma-Aldrich) was added and stirred for 30 min to obtain a homogeneous white mixture. The solution was transferred to a 250 mL Teflon-lined autoclave, and the temperature was maintained at 180 °C for 36 h before being cooled to room temperature. Centrifugation was used to collect the resulting white precipitate several times using deionized water and absolute ethanol. After drying at 80 °C for 6 h and annealing at 550 °C for 4 h under an Ar atmosphere, the final product of Ag-decorated ZnO porous nanosheets (Ag-ZnO PNSs, thickness ~80 nm) was obtained. Additionally, we prepared bare ZnO porous nanosheets (ZnO PNSs, thickness ~80 nm) and ZnO nanoparticles (ZnO NPs) and compared their sensing properties to those of the Ag-ZnO PNSs treated with Li-ion insertion/extraction. ZnO NPs were synthesized using the hydrothermal method previously described in our reports [25]. As shown in the SEM image in Fig. S1, the average particle size of the spherical ZnO NPs was ~20 nm.

2.2. Fabrication of coin-cell assembly

We assembled Li coin cells to implant Li ions into the as-synthesized Ag-ZnO PNSs. Cu foil coated with Ag-ZnO PNSs and an Li foil were used as the anode and cathode of the coin-cell assembly, respectively. Slurry casting was used to fabricate the anode of the Ag-ZnO PNS-coated Cu foil. The slurry material was prepared by mixing the active and conductive material, and binder with the dispersion solution. To increase the conductivity of the active material, carbon black (Super P® Conductive, Timcal Graphite & Carbon) was used as a conductive material. Polyvinylidene fluoride (PVDF, Mw ~534,000) was used as a binder to aid in the adhesion of the active material and conductive material to a Cu foil. In a mortar containing a certain amount of N-methyl pyrrolidone, Ag-ZnO PNSs (94 wt%) were mixed with 3 wt% carbon black and 3 wt% PVDF. The as-prepared slurry was then coated on a copper foil and dried in a vacuum oven at 60 °C for 12 h. The as-fabricated electrodes were cut to a 1 cm^2 (1 cm × 1 cm) size and used as the anode.

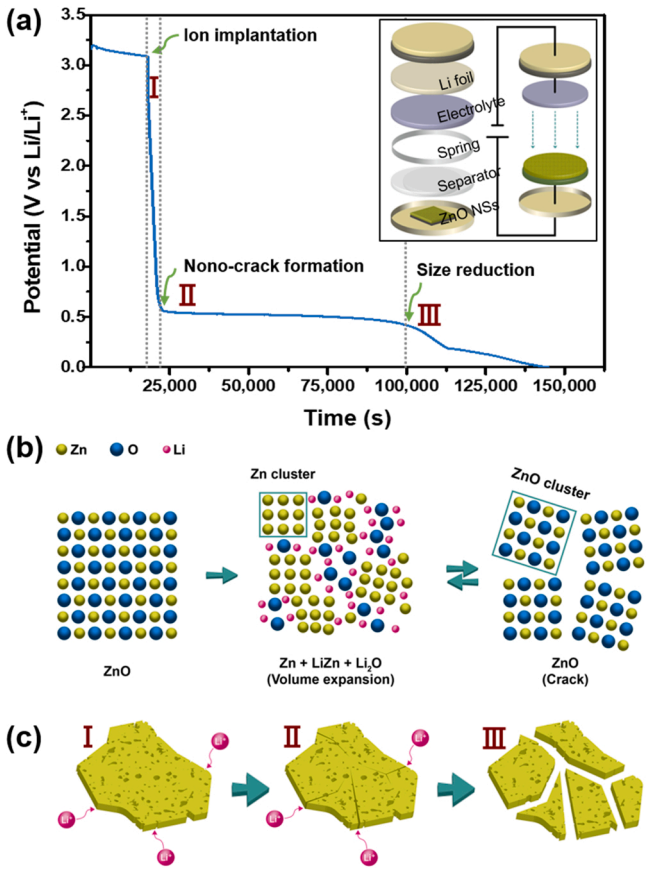

Fig. 1. (a) Galvanostatic discharge curve of Ag-ZnO PNSs/Li cell. The insert is a schematic of the coin cell assembly process and Li-ion discharge. (b) Schematic illustration of the electrochemical reactions between ZnO and Li. (c) Schematic diagram of morphological changes with increasing amount of implanted Li ions, corresponding to the specified I, II, and III states in the voltage profile in (a).

The electrolyte of the coin cell was prepared by combining 1 M $LiPF_6$ with ethylene carbonate and diethyl carbonate in a 1:1 wt ratio. In the cell, commercial polyethylene was used as a separator between the cathode and anode materials. Finally, as shown in the inset of Fig. 1, a CR 2032-type coin cell was assembled in an Ar glove box in the order of the anode (Cu foil coated with Ag-ZnO PNSs), separator, electrolyte, and cathode (Li foil).

2.3. Li-ion implantation

A galvanostatic charge-discharge method was used to implant Li-ions. A constant current (−100 μA/cm^2) was applied to the assembled coin cell over time to determine the potential difference generated between the anode and cathode. Charge-discharge cycles were conducted on the solid-state cells using a charge/discharge instrument (WonATech, WBCS3000L32). The Cu foil coated with the electrode material containing Ag-ZnO PNSs was washed three times with acetone, deionized water, and acetic acid (1 mM) following the charge-discharge process, and then the Ag-ZnO PNS powder was separated from the copper foil. The precipitated powder was dried under vacuum for 12 h at 60 °C.

2.4. Material characterization

The crystalline phases of ZnO-based samples were analyzed using an X-ray diffractometer (XRD, SmartLab, Rigaku) with Cu Kα1 radiation ($\lambda = 1.5409$ Å). The morphology and microstructure of the samples were investigated using scanning electron microscopy (SEM, JEOL-7800 F, JEOL Ltd.), transmission electron microscopy (TEM, Talos F200X, FEI), and scanning transmission electron microscopy (STEM, FEI Talos F200X TEM) equipped with energy dispersive X-ray spectroscopy (EDS). X-ray photoelectron spectroscopy (XPS, Thermo Fisher Scientific Co.) with Al Kα radiation (1486.6 eV) was used for the chemical state analysis of the surface. Photoluminescence (PL) spectra of the samples were obtained at room temperature using a micro-Raman spectrometer (Horriba Jovin Yvon) with a 325-nm He–Cd laser as an excitation source. The specific surface area was obtained using Brunauer-Emmett-Teller analysis (BET, TriStar II 3020, Micromeritics Instrument Corporation) through nitrogen adsorption-desorption at 77 K.

2.5. Fabrication of sensor devices

Various as-prepared powders were cast on interdigitated Pt electrodes to fabricate sensor devices. Interdigitated Pt electrodes were patterned on a SiO_2 substrate (8.5 × 8.5 mm) in detail. After dissolving the powders in ethanol, they were dropped on the Pt electrodes. Finally, the sensor devices were dried at 100 °C and annealed at 550 °C for 2 h to remove the solvent and to improve the mechanical and thermal stability of the sensing materials.

2.6. Gas sensing measurements

The sensing performance of the as-prepared samples for acetone was determined using a tube furnace sensing measurement system equipped with mass flow controllers (MFCs). By controlling the gas flow rate using MFCs, the acetone concentration was adjusted using synthetic air as the balance gas. The sensing chamber was then filled with a predetermined amount of acetone gas and synthetic air at a constant flow rate of 1000 sccm. The temperature controller of the tube furnace was used to change the operating temperature of the sensor. The sensing performance of the samples was examined for various acetone concentrations ranging from 0.1 to 10 ppm at working temperatures ranging from 250 to 500 ℃. The electrical sensing resistance of the sample was measured using a nanovoltmeter (Keithley 2182) at a time interval of 1 s using a current source and a constant current of 10 nA (Keithley 6220). The sensing response of the sample was determined from the definition of $(R_a - R_g)/R_g$, where $\Delta R = (R_a - R_g)$, where R_a and R_g are the sensor resistances in air and acetone gas, respectively. To test the selectivity for acetone detection, the sensor response to 10 ppm acetone was compared with those of several different interfering gases with concentrations of 10 ppm at the same operating temperature. H_2S, isoprene, ethanol, and benzene were each injected to the sensor, with synthetic air as a carrier and balance gas.

3. Results and discussion

The electrochemical properties of the Ag-ZnO PNSs were investigated during the charge-discharge cycle. The galvanostatic discharge curve induced by the change in potential difference was obtained when a constant current density of –100 μA/cm^2 was applied to the Ag-ZnO PNSs/Li cell, as shown in Fig. 1(a). A potential change was observed in three steps by continuous injection of Li ions. An abrupt decrease appeared from ~3 V to ~0.6 V (I-state), followed by a slow decrease of potential from ~0.6 V to ~0.4 V (II-state). It is then followed by a two-step decrease of potential from ~0.4 V to ~0.2 V (III-state) and from 0.2 V to 0 V. The insertion of Li ions into the lattice of the Ag-ZnO PNSs is responsible for the sharp decrease in the I-state. As the amount of implanted Li ions increased, some defects or cracks formed on the Ag-ZnO PNSs (stage II). According to the literature [26], in the discharging II state, a two-step electrochemical reaction occurs between ZnO and Li, which can be written as.

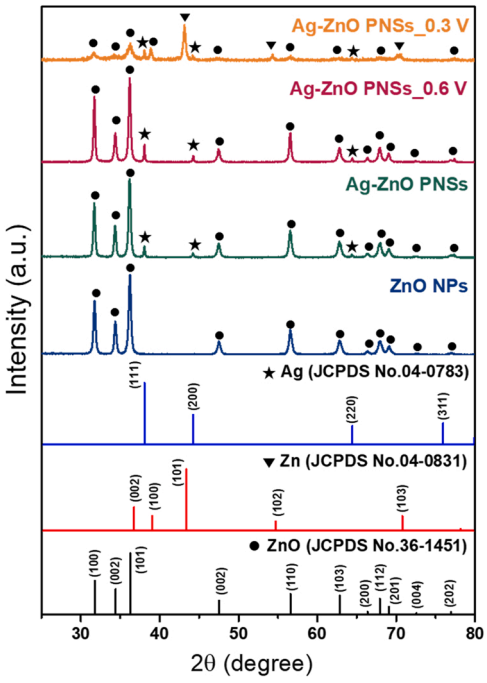

Fig. 2. XRD patterns of ZnO NPs, Ag-ZnO PNSs, Ag-ZnO PNSs_0.6 V, and Ag-ZnO PNSs_0.3 V.

$$ZnO + 2Li \rightarrow Zn + Li_2O \quad (1)$$

$$Zn + Li \rightarrow LiZn \quad (2)$$

Subsequently, two reversible reactions arise during the change-discharge process as follows:

$$LiZn \leftrightarrow Zn + Li \quad (3)$$

$$Zn + Li_2O \leftrightarrow ZnO + 2Li \quad (4)$$

Fig. 1(b) depicts in brief, the electrochemical reactions between ZnO and Li during the charging-discharging process. A large tensile stress was applied to the ZnO PNSs as a result of the lithiation/delithiation process, and nanocracks were partially generated and propagated along the {0001} or {11$\bar{2}$2} cleavage planes of ZnO PNSs (II-state in Fig. 1(b)) [24,26]. The nano-cracks were subjected to large lattice deformation between ZnO and Zn as the amount of Li ions increased, resulting in fracture and size reduction (state III in Fig. 1(c)). To investigate the effect of Li-ion insertion/extraction on the microstructure of the Ag-ZnO PNSs, we prepared the intrinsic Ag-ZnO PNSs and Ag-ZnO PNSs samples treated with discharging voltages of 0.6 V (Ag-ZnO PNSs_0.6 V) and 0.3 V (Ag-ZnO PNSs_0.3 V), which correspond to II and III states, in the electrochemical potential profiles, respectively.

XRD was used to examine the changes in the crystalline structure of various as-prepared Ag-ZnO PNSs before and after Li-ion implantation. Furthermore, the crystalline phases of the Ag-ZnO PNS samples were compared to those of the pristine ZnO NPs. The XRD patterns of ZnO NPs, Ag-ZnO PNSs, Ag-ZnO PNSs_0.6 V, and Ag-ZnO PNSs_0.3 V are shown in Fig. 2. The XRD diffraction peaks of all samples are well indexed to the hexagonal wurtzite ZnO phase (JCPDS No. 36-1451) with no other impurity phases. In addition, no Li XRD diffraction peaks are observed in the Li-ion treated samples. During washing, the Li ions that remain after the electrochemical reaction between ZnO and Li can be dissolved and removed. It should be noted that the Ag-ZnO PNS-based samples only showed diffractions with face-centered cubic symmetry

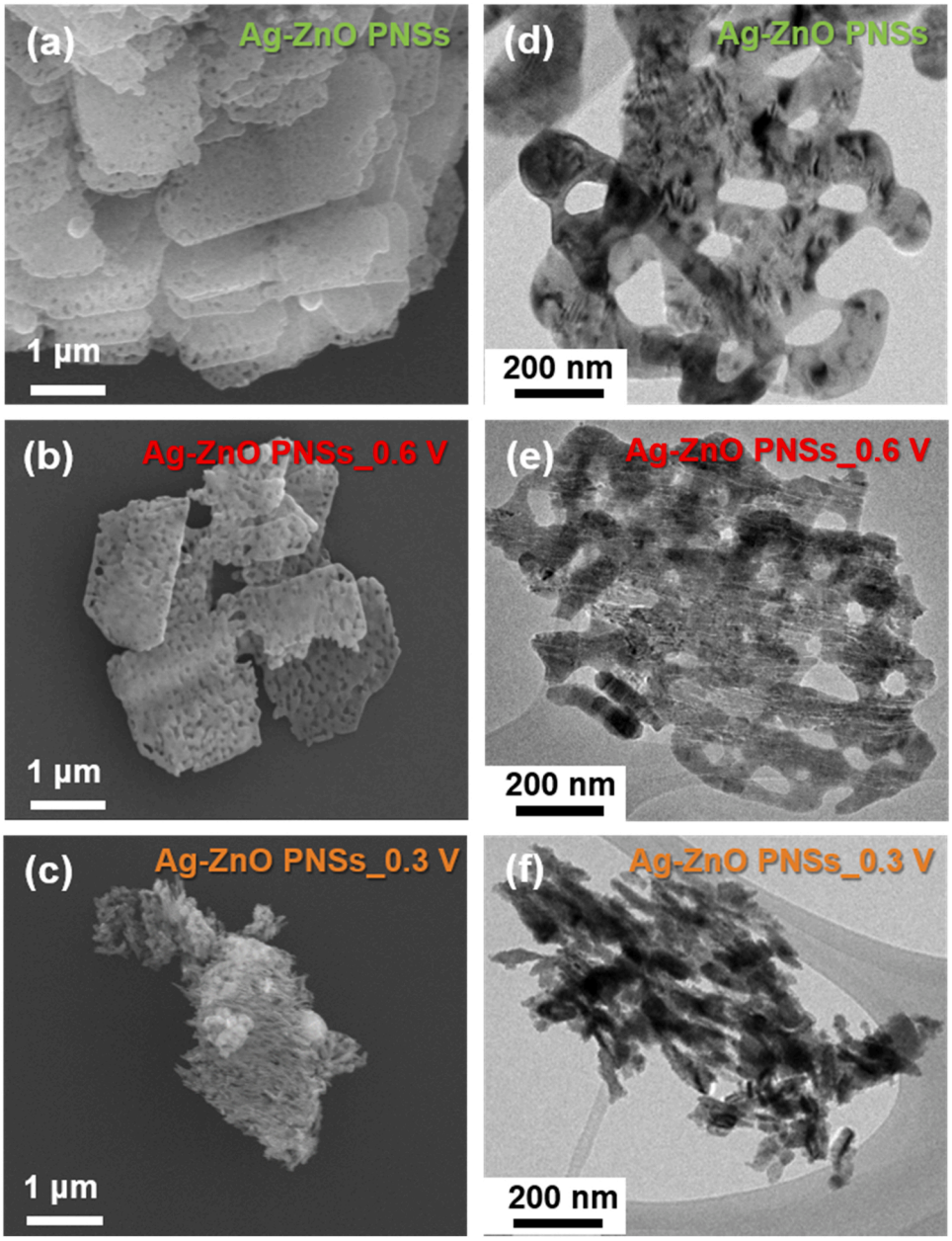

Fig. 3. (a)–(c) SEM images and (d)–(f) TEM images of Ag-ZnO PNSs, Ag-ZnO PNSs_0.6 V, and Ag-ZnO PNSs_0.3 V, respectively.

corresponding to the pure silver metal (JCPDS No. 04-0783). Furthermore, a lower angular shift in the peak positions of the ZnO phase, which could be induced by volume expansion owing to the intercalated Li ions, was not observed in any of the Li-ion treated samples. Based on this evidence, we discovered that Ag particles were decorated and segregated in the grain boundaries of ZnO crystallites rather than displacing Zn^{2+} and integrating into the ZnO lattice. The XRD data of Ag-ZnO PNSs_0.3 V revealed the presence of metallic Zn with hexagonal symmetry (JCPDS No. 04-0831), which accounted for more than 52 % of the weight fraction when compared to the ZnO phase. Additionally, the peak intensity was significantly reduced, and a broadening of the peak was also observed, indicating the deterioration of crystallinity due to size reduction. The results show that a potential of 0.3 V provides a significant amount of Zn conversion and size reduction of ZnO.

The morphology and microstructure changes of the intrinsic Ag-ZnO PNSs were studied using electron microscopic analysis SEM and TEM. Fig. 3(a)–(c) show the SEM images of Ag-ZnO PNSs, Ag-ZnO PNSs_0.6 V, and Ag-ZnO PNSs_0.3 V, respectively. The TEM images of the isolated NSs are shown in Fig. 3(d)–(f). The hydrothermally synthesized pristine samples were superimposed on each other in several layers, as shown in Fig. 3(a) and the aggregated size was approximately 10–15 μm. The overlapped ZnO PNSs were separated after the Li-ion implantation process, but a porous surface was still observed, indicating that the integrity of the porous structure was intact (Fig. 3(b) and Fig. 3(c)). However, as shown in the TEM images (Fig. 3(e) and 3(f)), the Ag-ZnO PNS samples treated with Li-ion insertion/extraction have unique characteristics. Cracks propagate through the surface of the isolated Ag-ZnO PNSs_0.6 V, which has an average size of 1–2 μm in length, (indicated by bright gray lines in Fig. 3(e)). In addition, a significant decrease in size below 200 nm was observed for the Ag-ZnO PNSs_0.3 V, as shown in Fig. 3(f)). According to the electrochemical reactions described in Fig. 1, the potentials of 0.6 V and 0.3 V for the Ag-ZnO PNSs caused crack formation and size reduction, respectively.

The non-cracked and cracked regions of Ag-ZnO PNSs_0.6 V were further characterized using microstructural analysis. Fig. 4(a) and 4(b) show HR-TEM images of the nano-scale cracked Ag-ZnO PNSs

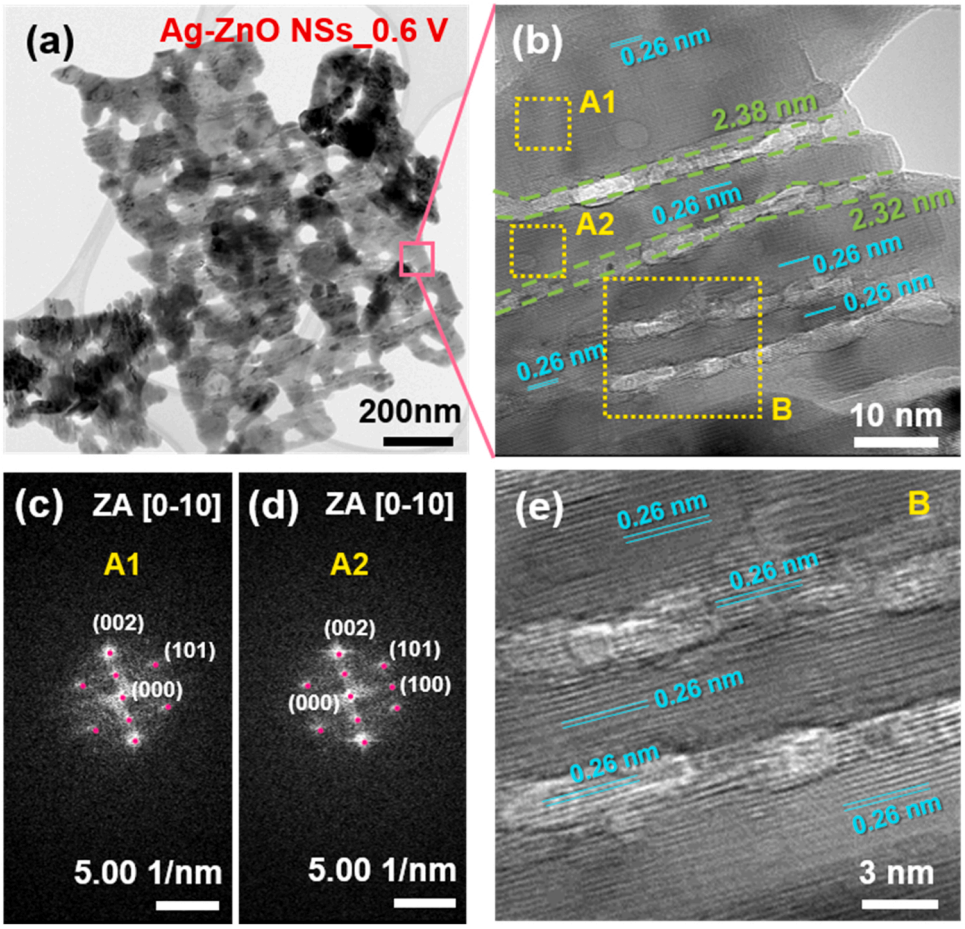

Fig. 4. TEM analysis of Ag-ZnO PNSs_0.6 V. (a) Low- and (b) High-magnification HR-TEM image. FFT patterns in the region of (c) A1 and (d) A2 shown in (b). (e) HR-TEM image in the region of B shown in (b).

discharged at 0.6 V, at low and high magnifications, respectively. All over the non-cracked region (Fig. 4(b)), lattice fringes with a spacing of 0.26 nm corresponding to the (002) plane of hexagonal wurtzite-type ZnO were observed. In addition, the fast Fourier transformation (FFT) patterns performed on selected regions of A1 (Fig. 4(c)) and A2 (Fig. 4 (d)) for a zone axis [0–10] showed that the Ag-ZnO PNSs_0.6 V was well crystallized. When combined with FFT analysis, it is confirmed that the crystallinity of Ag-ZnO PNSs is well maintained without lattice deformation of ZnO, even when tensile stresses are generated during the Li-ion insertion/extraction process, which is consistent with the XRD results (Fig. 2). The cracks were distributed over the surface of the PNSs with an average width of 2.3 nm as shown in Fig. 4(b). The magnified HRTEM image of region B in Fig. 4(e) shows that the cracked regions have the same *d*-spacing as the ZnO lattice fringe, but the lattice fringes are partially deteriorated. Therefore, the cracked region can be identified as the ZnO phase-containing defects. The brighter region in the nanocracks, on the other hand, cannot be a ZnO phase. The presence of ZnO was not detected by the EDS spectral analysis in some areas of the cracked region, (Figs. S2(a) and S2(b)). Therefore, it was confirmed that crystal defects and nanogaps coexist in the cracked region in the Ag-ZnO PNSs_0.6 V.

The elemental distribution of Ag-ZnO PNSs_0.6 V was investigated using STEM equipped with EDS. A high-angle annular dark field (HAADF) STEM image of Ag-ZnO PNS _0.6 V is shown in Fig. 5(a). Fig. 5 (b)–(e) show the corresponding EDS mapping images for the total constituent elements, Zn, O, and Ag. The Zn (Fig. 5(c)) and O (Fig. 5(d)) mapping images clearly show the crack pattern, as shown in the HAADF image. As shown in Fig. 4(f), the nanocracks in Ag-ZnO PNSs_0.6 V contain very little Zn and O. The results show that the nanocracks were formed in the Ag-ZnO PNSs discharged at 0.6 V. Furthermore, Fig. 5(b) and 5(e) show that Ag nanoparticles with an average size of 2–5 nm are uniformly distributed across the surface of PNSs, but some are aggregated to a size of 15 nm or larger. As a result of the phase and microstructure analysis, it was confirmed that the Li-ion implantation process with different discharge voltages produces different microstructures on the Ag-ZnO PNSs: nanocrack formation for 0.6 V, and size reduction and Zn formation for 0.3 V.

XPS analysis was used to determine the surface chemical state of the as-prepared materials, particularly the oxygen states that have the greatest effect on sensing properties. Because the binding energy measured using XPS is the unique energy of the element, it is possible to analyze the elements in the sample. As the binding energy varies with the chemical binding state, information on the latter can be obtained. Thus, XPS simultaneously provides chemical information on the chemical structure and oxidation state of the sample component atoms. Fig. 6 shows the XPS spectra of the O 1 s state for ZnO NPs, Ag-ZnO PNSs, Ag-ZnO PNSs_0.6 V, and Ag-ZnO PNSs_0.3 V. As shown in Fig. 6, the XPS O1s peaks of the samples were deconvoluted into three individual quasi-Gaussian peaks centered on ~530 eV (red line), ~531 eV (orange line), and ~532 eV (green line). The low-energy curve is associated with the lattice oxygen in the ZnO structure, and the high-energy curve is attributed to the presence of loosely bound oxygen on the surface, such as in H_2O and OH groups [27]. The intermediate-energy curve corresponds to oxygen ions in oxygen-deficient regions [27]. The peak of the oxygen vacancies in the XPS profile does not correspond to the signal from the vacancies because an absent atom cannot have a signal in the

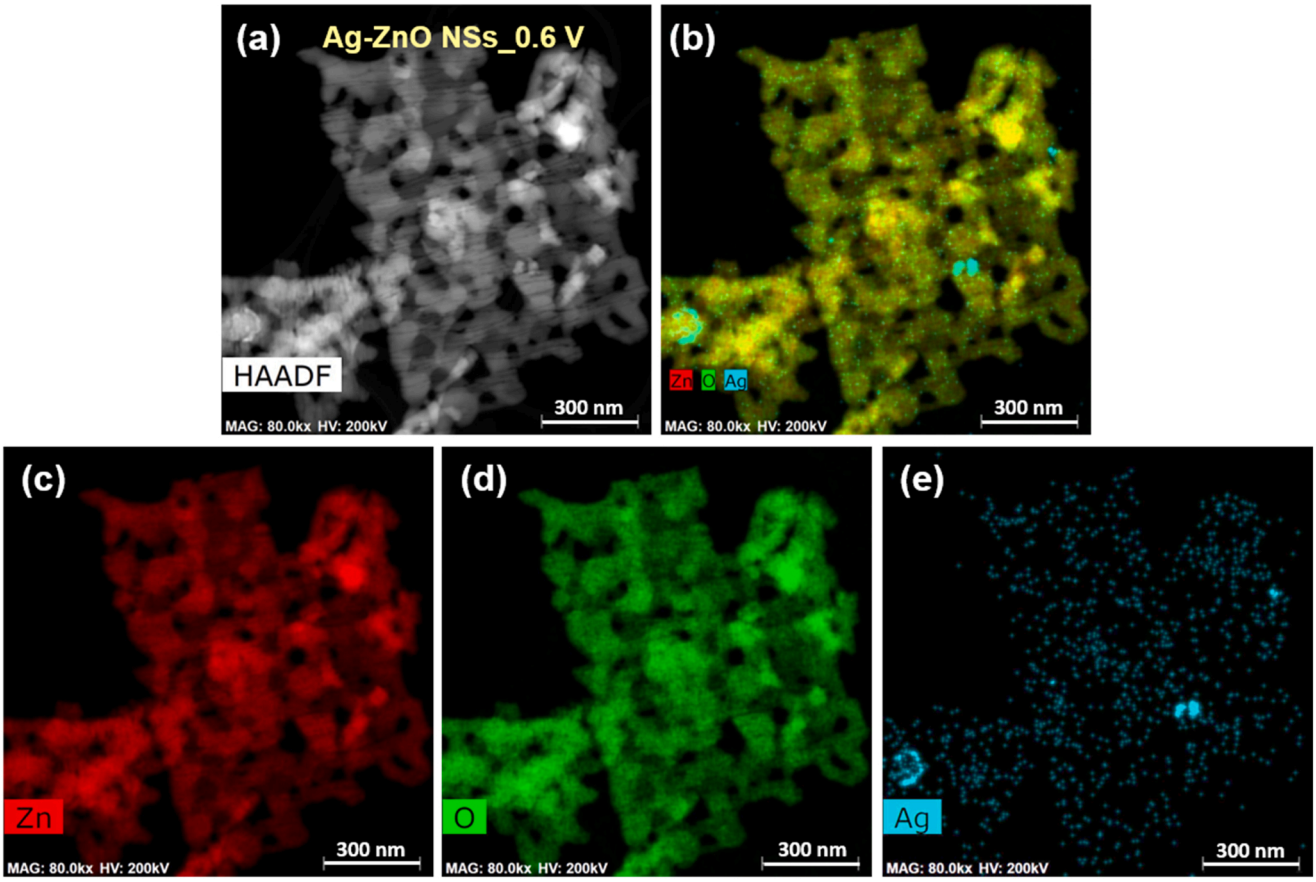

Fig. 5. (a) HAADF-STEM and (b)–(e) corresponding STEM-EDS elemental mapping images of Ag-ZnO PNSs_0.6 V.

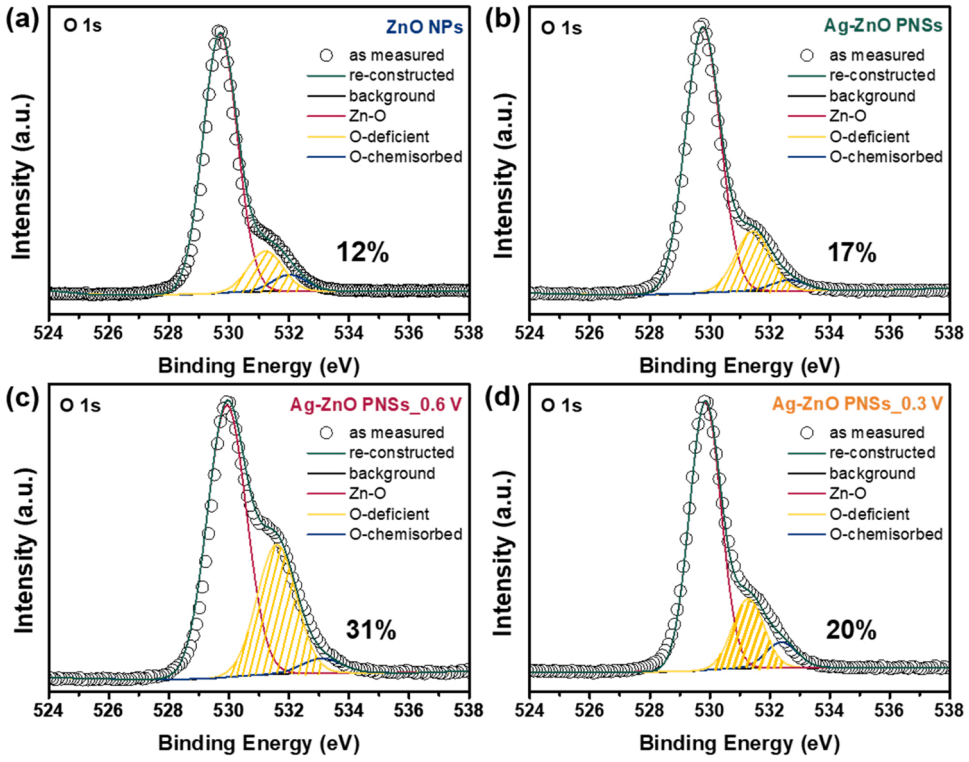

Fig. 6. Deconvoluted XPS O 1 s spectra of (a) ZnO NPs, (b) Ag-ZnO PNSs, (c) Ag-ZnO PNSs_0.6 V, and (d) Ag-ZnO PNSs_0.3 V.

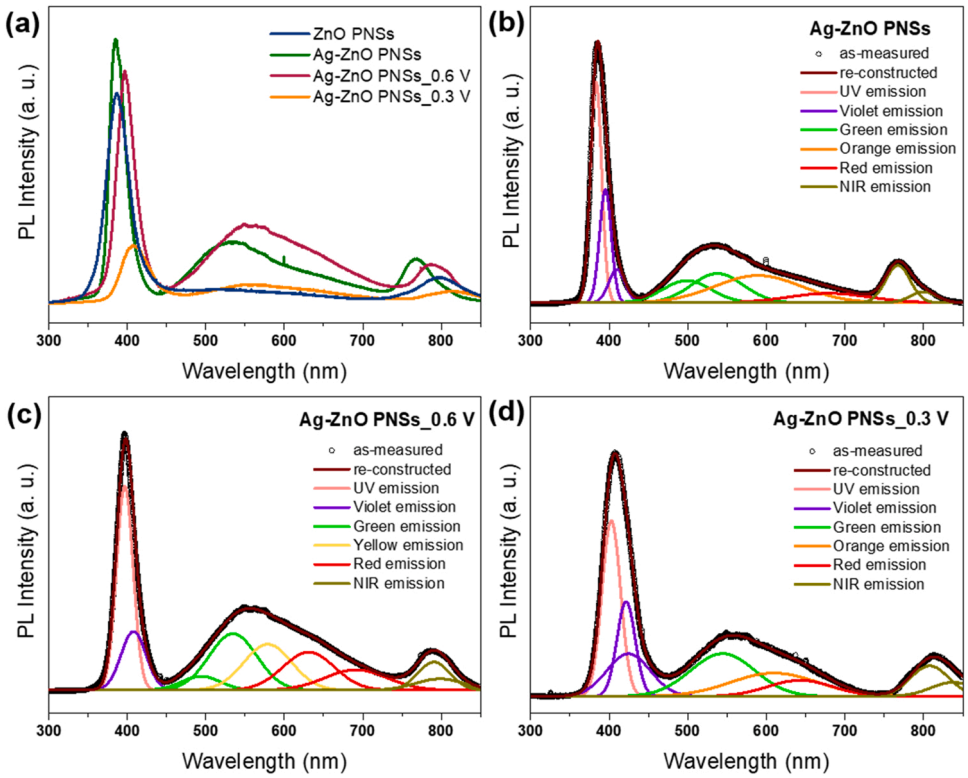

Fig. 7. (a) Room-temperature PL spectra of ZnO PNSs, Ag-ZnO PNSs, Ag-ZnO PNSs_0.6 V, and Ag-ZnO PNSs_0.3 V. Gaussian deconvolution of the PL band for (b) Ag-ZnO PNSs, (c) Ag-ZnO PNSs_0.6 V, and (d) Ag-ZnO PNSs_0.3 V.

XPS profiles. However, it can be assigned to the lattice oxygen ions (O^{-2}) bonded to the lower-valence cation (O^{-}). The cations have an oxidation state lower than that of the chemical formula. Such cations are responsible for maintaining the charge balance in the structure, thereby ensuring the presence of oxygen vacancies. Therefore, an unusual and asymmetric signal for an existing oxygen atom can be used as an indirect measure of the percentage of absent oxygen atoms.

Among the various oxygen states, oxygen vacancies are prevalent in this class of MOS and contribute significantly in improving the sensing performance of MOS [28]. They act as donors by transferring electrons from the MOS conduction band to adsorbed oxygen molecules, thereby promoting the ionization and chemisorption of oxygen ion species on the surface [28–30]. When exposed to the target gas, the oxygen ion species adsorbed on the sensing material's surface react with the target gas molecules. Therefore, the more oxygen vacancies there are, the stronger the response to the target gas. Therefore, the number of oxygen vacancies was estimated by calculating the area fraction of the O-deficient peak. The oxygen vacancies in ZnO NPs, Ag-ZnO PNSs, Ag-ZnO PNSs_0.6 V, and Ag-ZnO PNSs_0.3 V were ~12, ~17, ~31, and ~20 %, respectively.

The oxygen vacancies were also examined using PL. Fig. 7 displays the PL spectra of ZnO PNSs, Ag-ZnO PNSs, Ag-ZnO PNSs_0.6 V, and Ag-ZnO PNSs_0.3 V. All samples show a dominant sharp peak between 350 and 450 nm and a small broad peak between 750 and 800 nm. In particular, the Ag-ZnO PNS-based samples shows a broad peak between 450 and 750 nm. This is attributed to the intrinsic and extrinsic defects within the wurtzite structure of the ZnO PNSs [31,32]. As shown in Fig. 7(a), among the samples, Ag-ZnO PNSs_0.6 V showed more intense visible emission between 450 and 750 nm. This observation can be explained using the fact that surface dislocations could be one of the factors playing a role in the intense visible emission for the nanosheets [33]. The intense visible emission in Ag-ZnO PNSs_0.6 V could be caused by the formation of nanocracks through the surface, as can be seen in Figs. 3 and 4. In addition, Ag-ZnO PNSs_0.3 showed significantly reduced PL intensity and red-shift of the PL spectrum compared to other samples. This could be attributed to the reduced weight fraction of the ZnO phase and size reduction of ZnO PNSs, as observed in XRD results (Fig. 2).

To understand the optoelectronic states of the samples, we deconvoluted the entire range of spectra of the Ag-ZnO PNS-based samples via Gaussian fitting, as shown in Fig. 7(b)–(d). The PL spectrum can be deconvoluted into an ultraviolet (UV) emission peak centered at approximately 380 nm and visible emission peaks, violet, blue, green, yellow, orange, and red emissions in the wavelength ranges of 370–380, 380–449, 450–497, 498–569, 570–589, 590–619, and 620–750 nm, respectively [31,32]. The UV emission peak is associated with the near-band-edge emission due to recombination of free excitations, which is in agreement with the band gap of bulk ZnO [34]. The other emission peaks are attributed to zinc interstitials (Zn_i), extended zinc interstitials (ex-Zn_i denoted as both Zn_i^{+} and Zn_i^{++}), singly charged oxygen vacancies ($V_O^{\bullet}$), doubly charged oxygen vacancies ($V_O^{\bullet\bullet}$), and excess oxygen present on the sample surface [31,32,35]. The origin of the near-infrared (NIR) emission between 750 and 850 nm has been suggested to be an oxygen-related defect or a Zn interstitial [33]. Therefore, the visible and NIR emission peaks are closely related to the intrinsic and extrinsic defects of Ag-ZnO PNS-based samples. We estimated the area fraction of the deconvoluted green, yellow, orange, red, and NIR peaks, as presented in Table S1. Among these, green and yellow emission peaks are responsible for oxygen vacancies, which significantly affect the sensing properties of ZnO. The estimated area fraction of green and yellow peaks is 37 % for Ag-ZnO PNSs, 53 % for Ag-ZnO PNSs_0.6 V, and 39 % for Ag-ZnO PNSs_0.3 V. Thus, the result indicates that the amount of oxygen vacancies increases in the order of Ag-ZnO PNSs, Ag-ZnO PNSs_0.3 V, and Ag-ZnO PNSs_0.6 V, which is consistent with the XPS results (Fig. 6).

The N_2 adsorption-desorption method was used to estimate the specific surface area, which is another important material parameter that improves sensing performance. A greater specific surface area

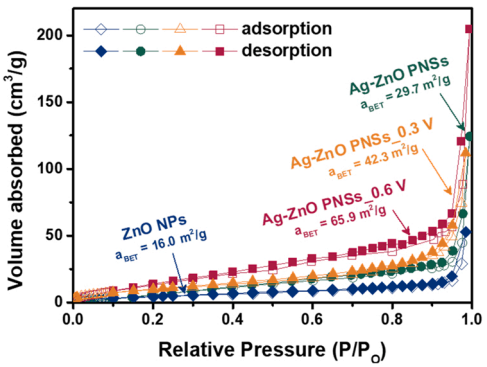

Fig. 8. N_2 adsorption-desorption isotherm of ZnO NPs, Ag-ZnO PNSs, Ag-ZnO PNSs_0.6 V, and Ag-ZnO PNSs_0.3 V.

indicates a greater number of N_2 absorption sites on the particle surface, resulting in a greater number of reactive sites for detecting the target gas. The N_2 adsorption–desorption isotherms of ZnO NPs, Ag-ZnO PNSs, Ag-ZnO PNSs_0.6 V, and Ag-ZnO PNSs_0.3 V are shown in Fig. 8. The BET specific surface area for the ZnO NPs, Ag-ZnO PNSs, Ag-ZnO PNSs_0.6 V, and Ag-ZnO PNSs_0.3 V was estimated from the N_2 adsorption branches and was determined to be approximately 16.0, 29.7, 65.9, and 42.3 m^2/g, respectively. The pore volumes of the PNSs were estimated to be ~0.079, ~0.314, and ~0.168 cc/g for Ag-ZnO PNSs, Ag-ZnO PNSs_0.6 V, and Ag-ZnO PNSs_0.3 V, respectively.

The sensing properties of the as-prepared samples were tested for detection of 10 ppm acetone at various operating temperatures ranging from 250° to 500°C. The sensing response curves of the ZnO NPs, ZnO PNSs, Ag-ZnO PNSs, Ag-ZnO PNSs_0.6 V, and Ag-ZnO PNSs_0.3 V to 10 ppm acetone at various operating temperatures are shown in Fig. 9. The sample response curves were obtained from the sensing resistance curves for 10 ppm acetone under various operating temperatures, as shown in Fig. S3. The figure indicates that the initial resistance of each sensor in air decreases with increasing temperature. This is attributed to the intrinsic properties of MOSs. In addition, a decrease of one to two orders of magnitude was observed for the sensor resistance in air using the Li-treated samples (Figs. S3(d) and (e)) compared with the bare samples (Figs. S3(a)–(c)). According to the XPS analysis, Li-ion treatment increases the number of oxygen vacancies (Fig. 6). The oxygen vacancies in ZnO behave as a donor and raise the position of the valence band, resulting in band gap narrowing [28,36,37]. Therefore, an increase in the number of electrons contributes to an increase in the electrical conductivity of ZnO with more oxygen vacancies. When a reducing gas is exposed to the sensor, the sensor resistance decreases

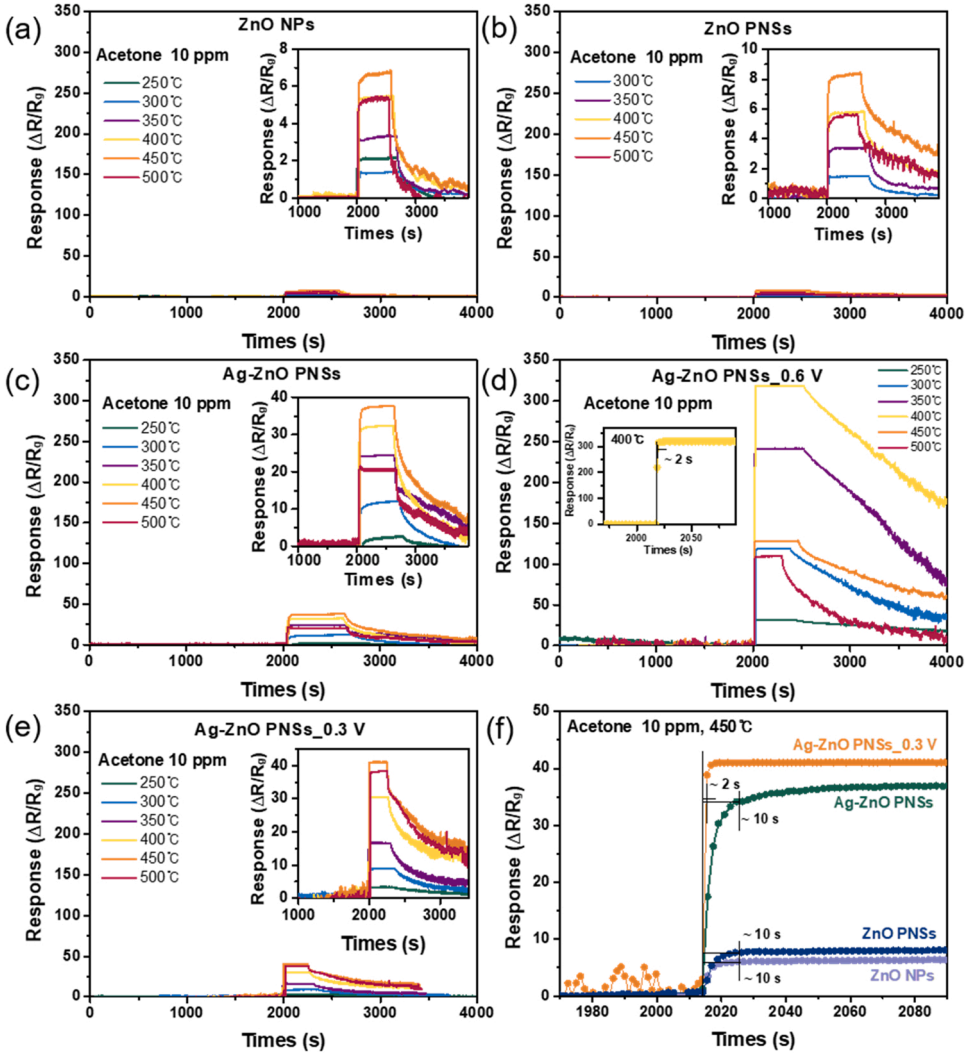

Fig. 9. Variation in the sensing response of (a) ZnO NPs, (b) ZnO PNSs, (c) Ag-ZnO PNSs, (d) Ag-ZnO PNSs_0.6 V, and (e) Ag-ZnO PNSs_0.3 V to 10 ppm acetone at various operating temperatures ranging from 250 to 500 ℃. (f) Response time of the ZnO NPs, ZnO PNSs, Ag-ZnO PNSs, and Ag-ZnO PNSs_0.3 V under exposure to 10 ppm acetone at their optimal operating temperature of 450 ℃. The response time of Ag-ZnO PNSs_0.6 V is displayed in the inset of Fig. 8(d).

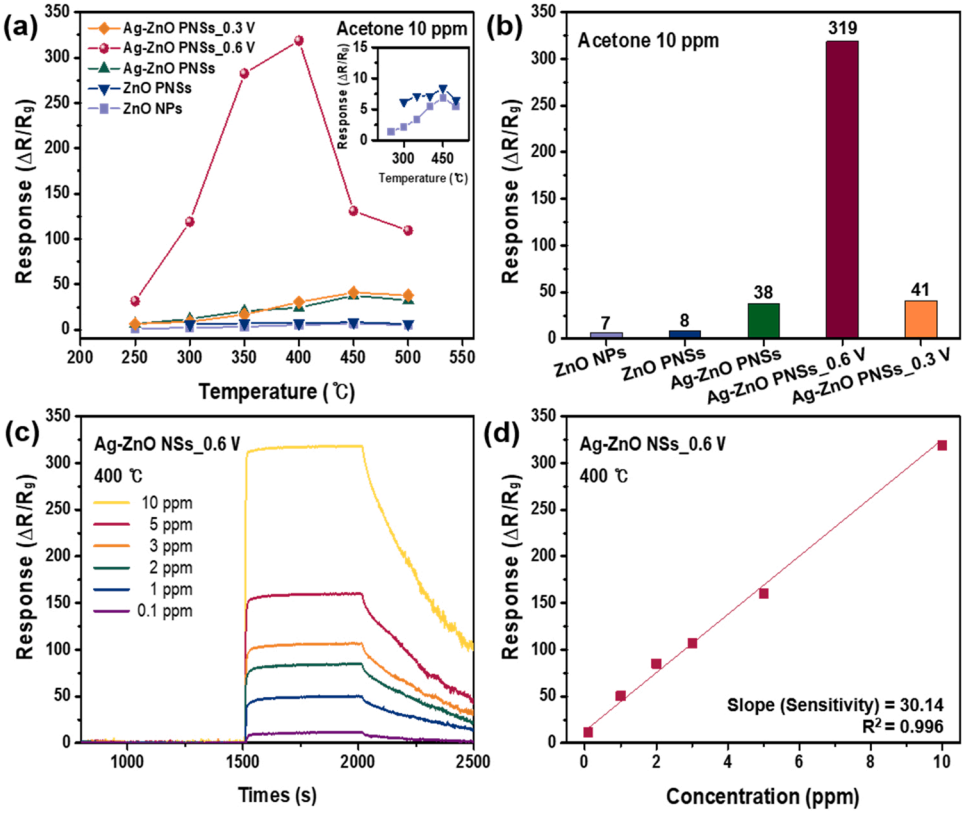

Fig. 10. (a) Maximum sensing response of ZnO NPs, ZnO PNSs, Ag-ZnO PNSs, Ag-ZnO PNSs_0.6 V, and Ag-ZnO PNSs_0.3 V to 10 ppm acetone as a function of operating temperatures. (b) Optimal sensing response of the samples obtained at each optimal operating temperature for the detection of 10 ppm acetone. (c) Variation in the sensing response of Ag-ZnO PNSs_0.6 V to various acetone concentration at an optimal operating temperature of 400 ℃. (d) Sensing response of Ag-ZnO PNSs_0.6 V as a function of acetone concentration in the range of 0.1–10 ppm at 400 °C. Sensitivity was calculated from the slope of a linear fit of the response.

because ZnO is an *n*-type semiconductor. Depending on the samples, different sensing performances were observed. The response times of the samples were estimated based on the time required for the sensor to achieve 90 % of the total response change for the target gas from the response curves exhibiting the highest sensing response at their optimal operating temperature. The results show that the samples treated with Li-ion implantation (Ag-ZnO PNSs_0.6 V and Ag-ZnO PNSs_0.3 V) have a response time of ~2 s, whereas the other samples have a response time of ~10 s (inset of Fig. 8(d) and Fig. 8(f)). However, all the samples exhibited long recovery times. This is a typical characteristic of MOS-based gas sensors. The reason for the long recovery time of MOS sensors is not well known; however, it may be due to its working principles. At the working temperature of the ZnO PNSs (400 °C), the O^{2-} species mainly interact with acetone according to the following equation [38]:

$$CH_3COCH_{3\ (ads)} + 8O_{(ads)}{}^{2-} \rightarrow 3CO_{2(gas)} + 3H_2O_{(gas)} + 16e^{-}. \quad (5)$$

Therefore, during the removal of the target gas, there is a possibility that CO_2 and H_2O gases, which are by-products of the chemical reaction between acetone and oxygen ion species, remain on the surface of the ZnO PNS, thus prolonging the recovery time.

The maximum sensing response to 10 ppm acetone as a function of operating temperature for various samples, including ZnO NPs, ZnO PNSs, Ag-ZnO PNSs, Ag-ZnO PNSs_0.6 V, and Ag-ZnO PNSs_0.3 V is shown in Fig. 10(a). For sensing 10 ppm acetone, the optimal operating temperature was 400 °C for Ag-ZnO PNSs_0.6 V, and 450 °C for ZnO NPs, ZnO PNSs, Ag-ZnO PNSs, and Ag-ZnO PNSs_0.3 V. The highest sensing responses of the samples at their optimal operating temperatures for 10 ppm acetone are summarized in Fig. 10(b), which were ~7, ~8, ~38, ~319, and ~41 for the ZnO NPs, ZnO PNSs, Ag-ZnO PNSs, Ag-ZnO PNSs_0.6 V, and Ag-ZnO PNSs_0.3 V, respectively. The ZnO PNSs decorated with Ag NPs demonstrated a higher response than the bare ZnO NPs and bare ZnO PNSs as shown in Fig. 10(b). The response values of bare ZnO NPs and bare ZnO PNSs were particularly similar. The bare ZnO PNSs have nearly identical morphology and microstructures (size of NSs, as well as size and density of pores) to the Ag-decorated ZnO PNSs (Fig. S4). Therefore, even though the PNSs are several μm in size, the Ag nanoparticles play an important role as a catalyst to greatly improve the

Table 1
Comparison of the sensing properties of various types of metal-oxide-based sensors for the detection of acetone.

Sensing material	Operating temperature (°C)	Concentration (ppm)	Response ($\Delta R/R_g$)	Sensitivity[a] (ppm^{-1})	Detection limit (ppm)	Response time (s)	Ref.
Ag-ZnO PNSs_0.6 V	400	10	319	31.9	0.1	2	This work
Ru-doped SnO_2 NFs	200	200	167	0.83	0.5	1	[39]
Pt-decorated Al-doped ZnO NPs	450	10	421	42.1	0.01	2.9	[40]
Pt-PS-WO_3 NFs	350	5	120	24	0.1	<32	[41]
Pt-loaded SnO_2 NTs	350	5	93	18.6	1	>120	[42]
Si-doped WO_3 NPs	400	0.6	4.5	7.5	0.02	>780	[43]
Co-doped WO_3 with carbon	50	4.5	4	0.9	0.5	>6	[44]
Al-doped ZnO NPs	500	1	12	12	0.01	11	[45]
CeO_2-ZnO NP	75	100	104	1.0	2	7	[46]
Hollow ZnO/MoS_2 core/shell	300	4.12	1	4.1	0.1	19	[47]

[a] sensitivity = response/concentration.

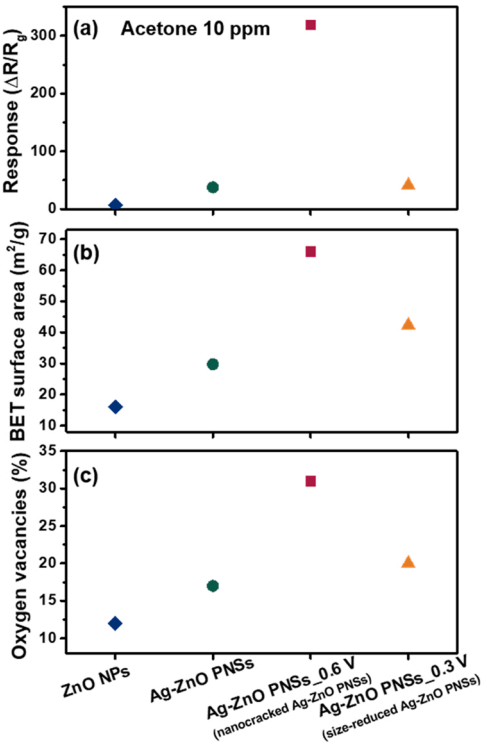

Fig. 11. Summary of the (a) sensing response, (b) BET surface areas, and (c) oxygen vacancies of ZnO NPs, Ag-ZnO PNSs, Ag-ZnO PNSs_0.6 V, and Ag-ZnO PNSs_0.3 V.

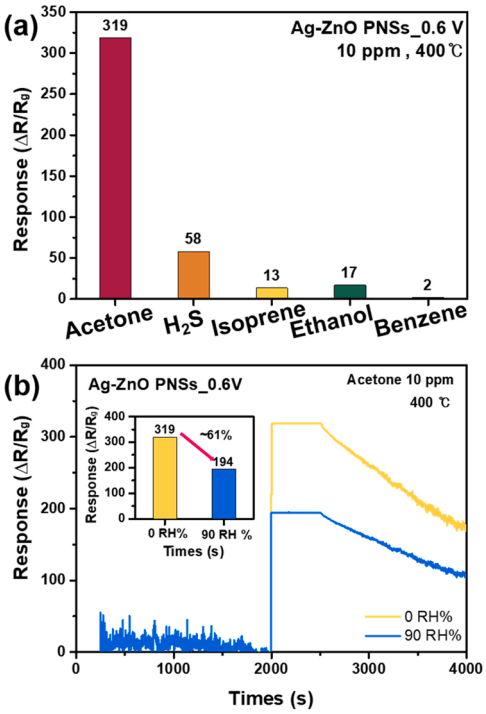

Fig. 12. (a) Sensing response of Ag-ZnO PNSs_0.6 V for 10 ppm of various gases including H_2S, isoprene, ethanol, and benzene. (b) Effect of humidity on sensing response of Ag-ZnO PNSs_0.6 V for 10-ppm acetone under conditions without humidity (dry, 0 % RH) and with 90 % RH.

acetone sensing performance. When compared to the other samples, the Ag-ZnO PNSs_0.6 V exhibits a superior sensing response at the relatively lower optimal operating temperature of 400 °C. At the optimal operating temperature, the sensing properties of Ag-ZnO PNSs_0.6 V with the highest sensing performance were investigated using different acetone concentrations. The variation in the sensing response of Ag-ZnO PNSs_0.6 V for different acetone concentrations at 400 °C is shown in Fig. 10(c). The Ag-ZnO PNSs_0.6 V exhibits a linear relationship between the range of 0.1–10 ppm, as shown in Fig. 10(d), with a high linear correlation coefficient of $R^2 = 0.996$. Therefore, the sensitivity (slope) of the sensor in the range of 0.1–10 ppm acetone was estimated to be ~30.14.

We further compared the acetone-sensing performance of Ag-ZnO PNSs_0.6 V with those of previously reported MOS-based gas sensors [39–47]. The sensing performance of Ag-ZnO PNSs_0.6 V was compared as the ratio of the response to the acetone concentration, as listed in Table 1. Ag-ZnO PNSs_0.6 V exhibited relatively high sensitivity, low detection limit, and fast response time.

The sensing response of the samples to 10 ppm acetone is summarized using chemical and physical characteristic values, which have a significant impact on sensing performance. The sensing response, oxygen vacancy content, and BET surface areas of ZnO NPs, Ag-ZnO PNSs, Ag-ZnO PNSs_0.6 V (nanocracked Ag-ZnO PNSs), and Ag-ZnO PNSs_0.3 V (size-reduced Ag-ZnO PNSs) are shown in Fig. 11. According to the microscopic analysis, it was confirmed that the Li-ion implanted Ag-ZnO PNSs at 0.6 V have nanocracks with a width of ~2.3 nm throughout the surface, while the Li-ion implanted Ag-ZnO PNSs at 0.3 V have the size-reduced PNSs. The sensing response of the samples followed the trend of oxygen vacancy ($V_O^{\bullet\bullet}$) and specific surface area (a_{BET}) as shown in Fig. 11. Therefore, the differences in sensing performances for different samples can be explained by increases in $V_O^{\bullet\bullet}$ and a_{BET}.

The intrinsic Ag-ZnO PNSs have larger $V_O^{\bullet\bullet}$ and a_{BET} than the ZnO NPs, despite the fact that the NSs are significantly larger than the NPs in size. This shows that the pore structure was effective in providing these properties at a higher level. Size-reduced Ag-ZnO PNSs, on the other hand, have higher $V_O^{\bullet\bullet}$ and a_{BET} than intrinsic Ag-ZnO PNSs due to the decrease in size. However, the two values of the size-reduced Ag-ZnO PNSs are lower than those of the nanocracked Ag-ZnO PNSs. The lower $V_O^{\bullet\bullet}$ of size-reduced Ag-ZnO PNSs is because the conversion to ZnO was much reduced while a larger fraction was transformed to Zn as observed in XRD (Fig. 2). The lower a_{BET} is due to a significant decrease in pore volume as the pore structure collapsed due to the size reduction. It should be noted that the nanocracked Ag-ZnO PNSs have the highest values of $V_O^{\bullet\bullet}$ and a_{BET} due to the presence of nanocracks containing defects distributed throughout the surface of the nanosheet and the highest pore volume.

As a result, even when compared to the much smaller ZnO NPs (~20 nm), the nanocracked Ag-ZnO PNSs (~2 μm) exhibited a remarkably high response. The excellent sensing performance of nanocracked Ag-ZnO PNSs is attributed to the increased number of $V_O^{\bullet\bullet}$ and specific area in the presence of nanocracks, as well as the catalytic effect of Ag NPs. Therefore, our findings show that the formation of nanocracks by Li-ion implantation is an effective way to simultaneously increase $V_O^{\bullet\bullet}$ and surface area of ZnO, while also significantly improving gas sensing performance by increasing the number of sensing reaction sites.

We investigated the sensitivity of the Ag-ZnO PNS _0.6 V to other interfering gases at the optimal operating temperature to test its usefulness in practical applications. At 400 °C, Fig. 12(a) depicts the sensing response of the Ag-ZnO PNSs_0.6 V toward 10 ppm of various exhaled gases of H_2S and isoprene, as well as indoor/industrial hazardous gases of ethanol and benzene. The sensing response can be preferentially attributed to large dipole moments in the molecular structure of the target gas [48]. The dipole moment of acetone (2.91D) is much higher than that of H_2S (0.98D), isoprene (0.25D), ethanol (1.60D), and benzene (0D). Therefore, when compared to the other gases, the Ag-ZnO PNSs_0.6 V exhibited a significantly higher response to acetone. This

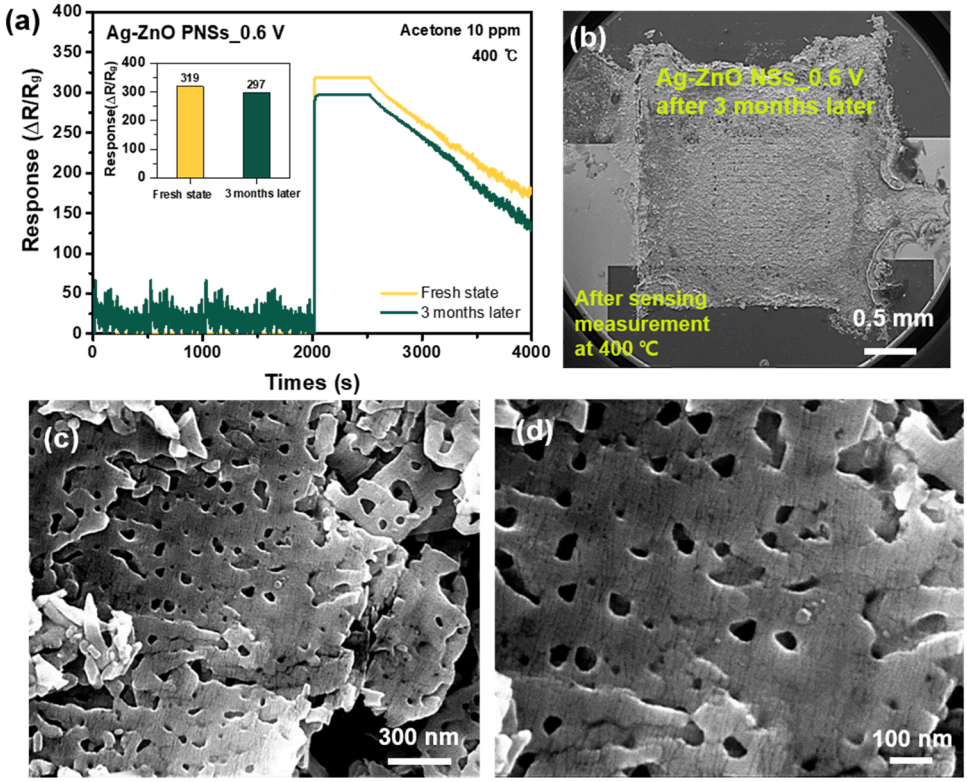

Fig. 13. Long-term stability of the sensing performance of Ag-ZnO PNSs_0.6 V: (a) Response curves of the sample prepared in the fresh state and stored state for 3 months after sensing measurement for the detection of 10 ppm acetone at 400 ℃. (b) SEM image of the sample cast on the interdigitated Pt electrodes after sensing measurement at 400 ℃, following 3 months of stored state. (c) Low and (d) high-magnification SEM image of the sample in (b).

indicates that the Ag-ZnO PNSs_0.6 V are extremely sensitive to acetone. Fig. 12(b) presents the effect of humidity on the sensing response of Ag-ZnO PNSs_0.6 V with 10 ppm of acetone under different humidity conditions (0 and 90 RH%) at the optimal working temperature of 400 °C. At a high humidity of 90 RH%, the response decreased to ~194, indicating ~61 % reduction in response to 10 ppm acetone. This implies that the sensing performance of Ag-ZnO PNSs_0.6 V at a high humidity is significantly degraded by the contamination of their reactive sites owing to the adsorption of water molecules. However, the degradation of sensing response due to high humidity can be prevented by employing a membrane moisture filter used in commercial gas sensors.

We also investigated the long-term stability of the Ag-ZnO PNSs_0.6 V for acetone sensing. The response curves of the Ag-ZnO PNSs_0.6 V prepared in the fresh state and stored for 3 months after sensing measurement for the detection of 10 ppm acetone at 400 °C, are shown in Fig. 13(a). After 3 months, the response to 10 ppm acetone decreased by ~7 % (~297) compared to the fresh state (~319). The microstructural changes that occurred as a result of sensing measurements were also investigated. SEM images of the sample cast on the interdigitated Pt electrodes after sensing measurement at 400 °C after 3 months of storage, are shown in Fig. 13(b)–(d). The SEM images show that the PNSs retain their structure without agglomeration (Fig. 13(c)) and the nanocrystals are still present on the surface of the PNS (Fig. 13 (d)), confirming the reliability and stability of the samples. Gas sensors based on MOS NPs have a problem in that the gas reactivity decreases significantly during repeated measurements due to agglomeration or aggregation, whereas the gas sensor based on nanocracked Ag-ZnO PNSs has a significant advantage as a sensing material because the nanocrack structures are preserved even after repeated measurements at high temperatures.

4. Conclusions

We present an innovative approach to defect engineering for improving the acetone sensing performance of ZnO-based sensors. To change the morphology and structure of the Ag-ZnO porous nanosheets, an electrochemical Li-ion implantation process was used. Nanocracks can be generated while the crystal structure of ZnO is preserved by controlling the discharge voltage. The nanocracks created activate the electron movement path further by increasing the number of oxygen vacancies and the specific surface area. The nanocracked Ag-ZnO porous nanosheets demonstrated an excellent sensing response (~319) to 10 ppm acetone and a low detection limit (0.1 ppm) at the optimum operating temperature of 400 °C due to this synergetic effect. Furthermore, it was discovered that the gas sensor based on nanocracked Ag-ZnO porous nanosheets has a significant advantage because the nanocrack structures are maintained even after repeated high-temperature measurements. Our findings indicate that Li-ion implantation is an effective method for improving the sensing performance of metal oxides.

CRediT authorship contribution statement

Minkyung Lee: Conceptualization, Investigation, Formal analysis, Visualization, Writing – original draft. **Hyun-Sook Lee:** Conceptualization, Validation, Writing – original draft, Writing – review & editing. **Min Young Kim:** Investigation, Visualization. **Kyu Hyoung Lee:** Conceptualization, Validation. **Wooyoung Lee:** Supervision.

Declaration of Competing Interest

The authors declare that they have no known competing financial interests or personal relationships that could have appeared to influence the work reported in this paper.

Data availability

Data will be made available on request.

Acknowledgements

This research was supported by the Technology Innovation Program ('20013621', Center for Super Critical Material Industrial Technology) funded by the Ministry of Trade, Industry & Energy (MOTIE, Korea), the Basic Science Research Program (2017M3A9F1052297), and the Priority Research Centers Program (2019R1A6A1A11055660) through the National Research Foundation of Korea (NRF), funded by the Korean Government (Ministry of Science and ICT). H.-S. Lee gratefully acknowledges the support from the Basic Research in Science and Engineering Program of the NRF (2021R1A2C1013690).

Appendix A. Supporting information

Supplementary data associated with this article can be found in the online version at doi:10.1016/j.snb.2022.132671.

References

[1] C. Deng, J. Zhang, X. Yu, W. Zhang, X. Zhang, Determination of acetone in human breath by gas chromatography–mass spectrometry and solid-phase microextraction with on-fiber derivatization, J. Chromatogr. B 810 (2004) 269–275.
[2] M. Righettoni, A. Tricoli, S. Gass, A. Schmid, A. Amann, S.E. Pratsinis, Breath acetone monitoring by portable Si:WO_3 gas sensors, Anal. Chim. Acta 738 (2012) 69–75.
[3] Q.A. Drmosh, I.O. Alade, M. Qamar, S. Akbar, Zinc oxide-based acetone gas sensors for breath analysis: a review, Chem. Asian J. 16 (2021) 1519–1538.
[4] T.-R. Rashid, D.-T. Phan, G.-S. Chung, A flexible hydrogen sensor based on Pd nanoparticles decorated ZnO nanorods grown on polyimide tape, Sens. Actuators B Chem. 185 (2013) 777–784.
[5] V. Galstyan, E. Comini, C. Baratto, G. Faglia, M. Brisotto, E. Bontempi, G. Sberveglieri, Growth and gas sensing properties of rough ZnO nanowires, in: Proceedings of the Foueteenth IMCS, International Meeting on Chemical Sensors (2012) 1623–1625.
[6] Y. Xiao, L. Lu, A. Zhang, Y. Zhang, L. Sun, L. Huo, F. Li, Highly enhanced acetone sensing performances of porous and single crystalline ZnO nanosheets: high percentage of exposed (100) facets working together with surface modification with Pd nanoparticles, ACS Appl. Mater. Interfaces 4 (2012) 3797–3804.
[7] X. Yu, F. Song, B. Zhai, C. Zheng, Y. Wang, Electro spun ZnO nanotubes and its gas sensing applications, Phys. E Low. Dimens. Syst. Nanostruct. 52 (2013) 92–96.
[8] S.B. Khan, M. Faisal, M.M. Rahman, A. Jamal, Low-temperature growth of ZnO nanoparticles: photocatalyst and acetone sensor, Talanta 85 (2011) 943–949.
[9] W. Li, X. Wu, N. Han, J. Chen, X. Qian, Y. Deng, W. Tang, Y. Chen, MOF-derived hierarchical hollow ZnO nanocages with enhancedlow-concentration VOCs gas-sensing performance, Sens. Actuators B Chem. 225 (2016) 158–166.
[10] N.H. Al-Hardana, M.J. Abdullah, A.A. Aziz, Performance of Cr-doped ZnO for acetone sensing, Appl. Surf. Sci. 270 (2013) 480–485.
[11] M.H. Darvishnejad, A.A. Firooz, J. Beheshtian, A.A. Khodadadi, Highly sensitive and selective ethanol and acetone gas sensors by adding some dopants (Mn, Fe, Co, Ni) onto hexagonal ZnO plates, RSC Adv. 6 (2016) 7838–7845.
[12] Y. Wang, X. Meng, J.-L. Cao, Rapid detection of low concentration CO using Pt-loaded ZnO nanosheets, J. Hazard. Mater. 381 (2020), 120944.
[13] C. Qin, B. Wang, P. Li, L. Sun, C. Han, N. Wu, Y. Wang, Metal-organic framework-derived highly dispersed Pt nanoparticles-functionalized ZnO polyhedrons for ppb-level CO detection, Sens. Actuators B Chem. 331 (2021), 129433.
[14] W. Baiqi, J. Liqiang, Q. Yichun, L. Shudan, J. Baojiang, Y. Libin, X. Baifu, F. Honggang, Enhancement of the photocatalytic activity of TiO_2 nanoparticles by surface-capping DBS groups, Appl. Surf. Sci. 252 (2006) 2817–2825.
[15] Y. Zhang, A. Kolmakov, S. Chretien, H. Metiu, M. Moskovits, Control of catalytic reactions at the surface of a metal oxide nanowire by manipulating electron density inside it, Nano Lett. 4 (2004) 403–407.
[16] W.W. Chow, S.W. Koch, Semiconductor-Laser Fundamentals: Physics of the Gain Materials, Springer, Berlin, 1999.
[17] S. Guha, J.M. Depuydt, M.A. Haase, J. Qiu, H. Cheng, Degradation of II-VI based blue-green light emitters, Appl. Phys. Lett. 63 (1993) 3107–3109.
[18] G. Lutz, Semiconductor Radiation Detectors: Device Physics, Springer, Berlin, 1999.
[19] S.R. Kurtz, A.A. Allerman, E.D. Jones, J.M. Gee, J.J. Banas, B.E. Hammons, InGaAsN solar cells with 1.0 eV band gap, lattice matched to GaAs, Appl. Phys. Lett. 74 (1999) 729–731.
[20] R. Wang, X. Chen, Z. Huang, J. Yang, F. Liu, M. Chu, T. Liu, C. Wang, W. Zhu, S. Li, S. Li, J. Zheng, J. Chen, L. He, L. Jin, F. Pan, Y. Xiao, Twin boundary defect engineering improves lithium-ion diffusion for fast-charging spinel cathode materials, Nat. Commun. 12 (2021) 3085.
[21] E. Uchaker, G.Z. Cao, The role of intentionally introduced defects on electrode materials for alkali-ion batteries, Chem. Asian J. 10 (10) (2015) 1608–1617.
[22] L. Pelaz, L.A. Marques, M. Aboy, P. Lopez, J. Barbolla, Atomistic modeling of dopant implantation and annealing in Si: damage evolution, dopant diffusion and activation, Comput. Mater. Sci. 33 (2005) 92–105.
[23] J. Gelpey, S. McCoy, A. Kontos, L. Godet, C. Hatem, D. Camm, J. Chan, G. Papasouliotis, J. Scheuer, in: Proceedings of the Extended Abstracts of the Eighth International Workshop on Junction Technology, IEEE, Shanghai, (2008), 82–86.
[24] D. Kim, S.H.R. Shin, Y. Kim, K. Crossley, Y. Kim, H. Han, J. Yoo, Hierarchical assembly of ZnO nanowire trunks decorated with ZnO nanosheets for lithium ion battery anodes, RSC Adv. 10 (2020) 13655–13661.
[25] A. Koo, R. Yoo, S.P. Woo, H.-S. Lee, W. Lee, Enhanced acetone-sensing properties of Pt-decorated Al-doped ZnO nanoparticles, Sens. Actuators B Chem. 280 (2019) 109–119.
[26] X.H. Huang, X.H. Xia, Y.F. Yuan, F. Zhou, Porous ZnO nanosheets grown on copper substrates as anodes for lithium ion batteries, Electrochim. Acta 56 (2011) 4960–4965.
[27] X.G. Han, H.Z. He, Q. Kuang, X. Zhou, X.H. Zhang, T. Xu, Z.X. Xie, L.S. Zheng, Controlling morphologies and tuning the related properties of nano/microstructured ZnO crystallites, J. Phys. Chem. C 113 (2009) 584–589.
[28] M. Al-Hashem, S. Akbar, P. Morris, Role of oxygen vacancies in nanostructured metal-oxide gas sensors: a review, Sens. Actuators B Chem. 301 (2019), 126845.
[29] L. Zhu, W. Zeng, Room-temperature gas sensing of ZnO-based gas sensor: a review, Sens. Actuators A Phys. 267 (2017) 242–261.
[30] L. Zhanga, Y. Yin, Large-scale synthesis of flower-like ZnO nanorods via a wet-chemical route and the defect-enhanced ethanol-sensing properties, Sens. Actuators B Chem. 183 (2013) 110–116.
[31] C. Singh, E. Panda, Variation of electrical properties in thickening Al-doped ZnO films: role of defect chemistry, RSC Adv. 6 (2016) 48910–48918.
[32] F. Kayaci, S. Vempati, I. Donmez, N. Biyikli, T. Uyar, Role of zinc interstitials and oxygen vacancies of ZnO in photocatalysis: a bottom-up approach to control defect density, Nanoscale 6 (2014) 10224–10234.
[33] A.B. Djurišić, Y.H. Leung, Optical properties of ZnO nanostructures, Small 2 (2006) 944–961.
[34] M.H. Huang, Y. Wu, H. Feick, G. Tran, E. Weber, P. Yang, Catalytic growth of zinc oxide nanowires by vapor transport, Adv. Mater. 13 (2001) 113–116.
[35] H. Zeng, G. Duan, Y. Li, S. Yang, X. Xu, W. Cai, Blue luminescence of ZnO nanoparticles based on non-equilibrium processes: defect origins and emission controls, Adv. Funct. Mater. 20 (2010) 561–572.
[36] H. Liu, F. Zeng, Y. Lin, G. Wang, F. Pan, Correlation of oxygen vacancy variations to band gap changes in epitaxial ZnO thin films, Appl. Phys. Lett. 102 (2013), 181908.
[37] S.A. Ansari, M.M. Khan, S. Kalathil, A. Nisar, J. Lee, M.H. Cho, Oxygen vacancy induced band gap narrowing of ZnO nanostructures by an electrochemically active biofilm, Nanoscale 5 (2013) 9238–9246.
[38] Z. Ahmad, A.Z. Sadek, K. Latham, J. Kita, R. Moos, W. Wlodarski, Chemically synthesized one-dimensional zinc oxide nanorods for ethanol sensing, Sens. Actuators B Chem. 187 (2013) 295–300.
[39] X. Kou, F. Meng, K. Chen, T. Wang, P. Sun, F. Liu, X. yan, Y. Sun, F. Liu, K. Shimanoe, G. Lu, High-performance acetone gas sensor based on Ru-doped SnO2 nanofibers, Sens. Actuators B Chem. 320 (2020), 128292.
[40] A. Koo, R. Yoo, S.P. Woo, H.-S. Lee, W. Lee, Enhanced acetone-sensing properties of pt-decorated al-doped ZnO nanoparticles, Sens. Actuators B Chem. 280 (2019) 109–119.
[41] S.-J. Choi, S.-J. Kim, W.-T. Koo, I.-I.-J. Cho, I.-D. Kim, Catalyst-loaded porous WO3 nanofibers using catalyst-decorated polystyrene colloid templates for detection of biomarker molecules, Chem. Commun. 51 (2015) 2609–2612.
[42] J.-S. Jang, S.-J. Kim, S.-J. Choi, N.-H. Kim, M. Hakim, A. Rothschild, I.-D. Kim, Thin-walled SnO2 nanotubes functionalized with Pt and Au catalysts via the protein templating route and their selective detection of acetone and hydrogen sulfide molecules, Nanoscale 7 (2015) 16417–16426.
[43] M. Righettoni, A. Tricoli, S.E. Pratsinis, Si: WO3 sensors for highly selective detection of acetone for easy diagnosis of diabetes by breath analysis, Anal. Chem. 82 (2010) 3581–3587.
[44] V. Saasa, T. Malwela, Y. Lemmer, M. Beukes, B. Mwakikunga, The hierarchical nanostructured Co-doped WO3/carbon and their improved acetone sensing performance, Mater. Sci. Semicond. Process. 117 (2020), 105157.
[45] R. You, Y. Park, H. Jung, H.J. Rim, S. Cho, H.-S. Lee, W. Lee, Acetone-sensing properties of doped ZnO nanoparticles for breath-analyzer applications, J. Alloy. Compd. 803 (2019) 135–144.
[46] J. Cui, G. Pan, X. Yang, M. Zhu, C. Huang, J. Qi, Enhanced acetone sensing performance of CeO2-ZnO at low temperature and its photo-excitation effect, Mater. Sci. Semicond. Process 118 (2020), 105221.
[47] X. Chang, X. Qiao, K. Li, P. Wang, Y. Xiong, X. Li, F. Xia, Q. xue, UV assisted ppb-level acetone detection based on hollow ZnO/MoS2 nanosheets core/shell heterostructures at low temperature, Sens. Actuators B Chem. 317 (2020), 128208.
[48] R. Yoo, A.T. Güntner, Y. Park, H.J. Rim, H.-S. Lee, W. Lee, Sensing of acetone by Al-doped ZnO, Sens. Actuators B Chem. 283 (2019) 107–115.

Minkyung Lee received her Master's degree in Materials Science and Engineering at Yonsei university in 2012. Since 2012, she is a senior researcher of Chem-bio Technology Center Team1 in Agency for Defense Development in Korea. She is currently a Ph.D. candidate at the Department of Materials Science and Engineering in Yonsei University under the supervision of Prof. Wooyoung Lee. She is currently studying on nanostructured metal-oxide semiconductor gas sensors.

Hyun-Sook Lee received a Ph.D. degree in Physics at POSTECH in 2008. Since 2015, she has been working as a research professor in the Department of Materials Science and Engineering at Yonsei University. Her research interests are in various materials related to high-temperature superconductors, solid-state hydrogen storages, rare-earth/rare-earth-free permanent magnets, nanostructured metal oxide semiconductor gas sensors, and Pd-based hydrogen sensors.

Min Young Kim is a Ph.D. candidate in the Department of Materials Science and Engineering at Yonsei University in Seoul, Korea. She received her Master's degree in the Department of Energy Science at Sungkyunkwan University in Suwon, Korea in 2018. Her research interests are bulk thermoelectric materials.

Kyu Hyoung Lee is currently an associate professor in the Department of Materials Science and Engineering at Yonsei University in Seoul, Korea. He received his Ph.D. in ceramic engineering from Yonsei University in 2005. From 2005–2007, he worked as a postdoctoral research fellow at Nagoya University. Since 2007, he has been a research staff member and since 2010 project leader at the Samsung Advanced Institute of Technology. His research activity has focused on the development of high-performance thermoelectric materials and functional oxides.

Wooyoung Lee is a professor of the Department of Materials Science and Engineering and the Director of Center for Super Critical Material Industrial Technology (MOTIE) at Yonsei University in Korea. He received a BS degree in Metallurgical Engineering in 1986, a MS degree in Metallurgical Engineering from the Yonsei University in 1988. He received a Ph. D. degree in Physics from University of Cambridge, United Kingdom in 2000. He is a regular member of National Academy of Engineering of Korea. He was a member of National Science & Technology Council and a director in Korea Israel Industrial R&D Foundation. In recent years, his research interests have centered on hydrogen sensors, various metal oxide semiconducting gas sensors, and breath analyzers. He is also studying thermoelectric materials and devices, and permanent magnets. He has received a number of awards in nano-related research areas and a Service Merit Medal (2008) from the Government of Korea due to contribution on the development of intellectual properties. He has authored and co-authored over 200 publications, and has edited three special books on nano-structured materials and devices.